

Circuit QED simulator of two-dimensional Su-Schrieffer-Hegger model: magnetic field induced topological phase transition in high-order topological insulators

Sheng Li,¹ Xiao-Xue Yan,¹ Jin-Hua Gao,^{1,2,*} and Yong Hu^{1,†}

¹*School of Physics, Huazhong University of Science and Technology, Wuhan, 430074, China*

²*Wuhan National High Magnetic Field Center, Huazhong University of Science and Technology, Wuhan 430074, China*

High-order topological insulator (HOTI) occupies an important position in topological band theory due to its exotic bulk-edge correspondence. Recently, it has been predicted that external magnetic field can introduce rich physics into two-dimensional (2D) HOTIs. However, up to now the theoretical description is still incomplete and the experimental realization is still lacking. Here we investigate the influence of continuously varying magnetic field on 2D Su-Schrieffer-Heeger lattice, which is one of the most celebrated HOTI models, and proposed a corresponding circuit quantum electrodynamics (cQED) simulator. Our numerical calculation shows that the zero energy corner modes (ZECMs), which can serve as evidence of the high order topology of the lattice, exhibit exotic and rich dependence on the imposed magnetic field and the inhomogeneous hopping strength. Moreover, by exploiting the parametric conversion method, we can establish time- and site-resolved tunable hopping constants in the proposed cQED simulator, thus providing an ideal platform for simulating the magnetic field induced topological phase transitions in 2D HOTIs. Since the high-order topological phases of the proposed model can be characterized by the existence of the ZECMs on the lattice, we further investigate the corner site excitation of the lattice in the steady state limit. Our numerical results imply that the predicted topological phase transitions can be unambiguously identified by the steady-state photon number measurement of the corner sites and their few neighbors. Requiring only current level of technique, our scheme can be readily tested in experiment and may pave an alternative way towards the future investigation of HOTIs in the presence of magnetic field, disorder, and strong correlation.

I. INTRODUCTION

High order topological insulator (HOTI) has attracted extensive research attention in the past few years due to its exotic boundary states [1, 2]. Generally speaking, a d -D n th-order HOTI has gapless $(d-n)$ -D boundary states, which is not only determined by but also a representation of its high order band topology [3–7]. A typical example is the 2D Su-Schrieffer-Heeger (SSH) lattice shown in Fig. 1a, which has four-site unit-cells coupled through homogeneous intra-cell hopping strength γ and inhomogeneous inter-cell hopping strengths λ_i [1, 8–10]. This lattice can host 0D zero-energy corner modes (ZECMs) instead of 1D gapless edge modes under certain circumstances, thus belonging to 2D second-order HOTI. Recently, the influence of external magnetic field on 2D HOTI has been investigated, and a variety of novel topological phases have been predicted [1, 11]. The motivation and the physics behind is that the imposed magnetic field can change the symmetry of the Hamiltonian [12]. It has been pointed out that the high-order topology of the 2D SSH model depends on both the uniformly-imposed plaquette magnetic field ϕ and the ratio λ_i/γ (Fig. 1a). For $\lambda_i > \gamma$ and $\phi = \pi$ [1, 13], this model enters the topological non-trivial region characterized by the appearance of ZECMs [14]. However, theoretical research up to now has focused only on several discrete values of the imposed

magnetic field, e.g., 0-flux and π -flux in Ref. [1] and $2\pi/3$ -flux and $2\pi/10$ -flux in Ref. [11]. The detailed and complete description of the role of magnetic field in HOTI is still lacking. From this point of view, building a corresponding analog quantum simulator [15] and investigating the behavior of the boundary states [16, 17] can offer insight and inspiration for further research. Meanwhile, despite the experimental progress of realizing HOTIs in various metamaterials [18–25], the proposed magnetic-field-induced topological phase transition has not been experimentally demonstrated yet, partially because the simultaneous realization of the site-dependent inhomogeneous hopping strength and the tunable synthetic gauge field is still challenging.

On the other hand, superconducting quantum circuit (SQC) has been regarded as a promising platform of realizing quantum simulation [26, 27]. The lattice sites in this setup are constructed by superconducting transmissionline resonators (TLRs) [28] and superconducting qubits, and electrons in conventional materials are replaced by microwave photons. Compared with other physical systems, SQC takes the advantage of flexible engineering of a large scaled lattice, which stems from the tunability and scalability in the circuit design and control [29]. With advances in theory and technology, the controllable coupling between SQC elements has been experimentally demonstrated [30, 31], leading to the on-demand synthesization of artificial gauge field [32] and many-body localization [33]. Moreover, the strong coupling between SQC elements [28, 34] allows the effective Kerr type [35] and Jaynes-Cummings-Hulbard type [36] nonlinearity and consequently the further simulation of

* jinhua@hust.edu.cn

† huyong@mail.hust.edu.cn

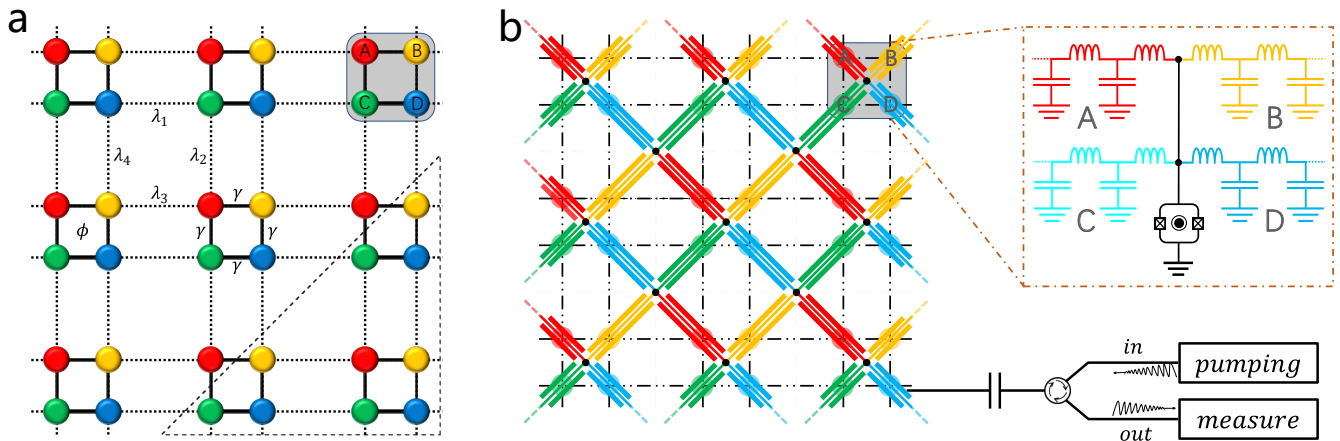


FIG. 1. **a** Sketch of the 2D SSH lattice composed of unit-cells with four sites labeled A—D (shadowed area). The lattice sites are coupled through uniform intra-cell coupling strength γ and inhomogeneous inter-cell coupling strengths λ_i . In each intra-cell plaquette, a uniform magnetic flux ϕ is penetrated. **b** Circuit QED simulator of the 2D SSH model. The lattice is built by TLRs grounded at their common ends (big dots) by coupling SQUIDs (crossed squares). The colors of the TLRs label their different eigenfrequencies. In the loop of each SQUID, an external time-dependent magnetic flux is penetrated to induce the tunable effective coupling between the neighboring TLRs.

strongly correlated photonic liquids [27, 37–40].

In this manuscript, we study the high order topology of 2D SSH lattice induced by continuously varying magnetic field and its quantum simulation in SQC system. In the first step, we propose a flexible circuit quantum electrodynamics (cQED) quantum simulator of 2D SSH lattice. Here the lattice sites are constructed by superconducting TLRs and coupled to their neighbors by grounding superconducting quantum interference devices (SQUIDs) (Fig. 1b). The photon hopping on this lattice is induced through the parametric modulation of the grounding SQUIDs [32, 41–43]. The distinct merit of this scheme is that it can provide time- and site-resolved tunability of both the hopping strengths and the hopping phases between the adjacent sites, thus enabling the simultaneous establishment of tunable inhomogeneous hopping strengths which is critical for the lattice to have non-trivial high order topology, and the non-trivial hopping phases which lead to controllable synthetic magnetic field for microwave photons.

The tunability of the proposed simulator in turn stimulates us to go beyond previous work [1, 11] and calculate the energy spectrum of the 2D SSH lattice versus continuous external magnetic field and the ratio between the intra- and inter-cell hopping strengths. Our results show that the spectrum and the ZECMs (and thus the high order topology of the lattice) exhibit rich and complicated behavior. In particular, the HOTI phase diagram of the lattice can be generally divided into five parts (see detailed discussion in Sec. III) based on the existence of the ZECMs. In certain phases regions, the non-trivial HOTI phase is robust against the imposed magnetic field, while in other regions the imposed magnetic field can lead to band gap closing and thus induce HOTI phase transition.

Our estimation based on recently reported experimental data [32, 41, 44–46] further pinpoints that the parameters of all the predicted HOTI phase regions can in principle be achieved in the proposed cQED simulator.

As the high order band topology of the proposed model can be characterized by the ZECMs, we further investigate the discrimination of the predicted HOTI phases through the corner-site pumping and the consequent steady-state photon number (SSPN) distribution measurement. The essential physics is that the spatial and spectral localization of the ZECMs can lead to exotic spatially localized SSPN distribution, and the latter can be used as strong evidence of the existence of the ZECMs. Our numerical results imply that with current level of technology, one can clearly identify the existence of the ZECMs and consequently the boundaries of the predicted HOTI phase regions by only measuring few sites near the corner. Our cQED architecture can therefore be regarded as an efficient platform of investigating the magnetic field effect on 2D HOTIs. Due to the flexibility and scalability offered by the SQC system, our proposal can be readily generalized to other HOTI lattice configurations [6, 47], and can allow the further incorporation of non-Hermiticity [48, 49], disorder [50], and strong correlation [27, 37–40], thus providing an alternative route of exploring HOTI in the future.

II. CIRCUIT QED LATTICE SIMULATOR OF 2D SSH MODEL

As shown in Fig. 1b, the proposed cQED lattice simulator is built up by four kinds of TLRs differed by their eigenfrequencies and placed in an interlaced square pat-

tern [42]. These four kinds of TLRs correspond to the A-D sublattice sites in Fig. 1a, respectively. In addition, we ground these TLRs at their common ends by grounding SQUIDs with effective Josephson inductances much smaller than those of the TLRs [41, 44]. The roles of the grounding SQUIDs are two-fold. Firstly, their small inductances impose shortcut boundary conditions for the TLRs. Due to the current dividing mechanism, a current flowing away from a particular TLR will prefer flowing to ground rather than to its neighbors [30]. Therefore, we can exploit the lowest $\lambda/2$ eigenmodes of the TLRs as the uncoupled localized Wannier modes of the lattice, and write the on-site part of the lattice Hamiltonian as

$$\mathcal{H}_S = \sum_{\alpha, \mathbf{r}} \omega_\alpha \alpha_{\mathbf{r}}^\dagger \alpha_{\mathbf{r}}, \quad (1)$$

where $\alpha_{\mathbf{r}}^\dagger/\alpha_{\mathbf{r}}$ are the creation/annihilation operators of the α th site in the \mathbf{r} th unit-cell for $\alpha \in A, B, C, D$, and ω_α are the corresponding eigenfrequencies. For the following establishment of the parametric frequency conversion (PFC) process, we further specified ω_α as $(\omega_A, \omega_B, \omega_C, \omega_D) = (\omega_0, \omega_0 + \Delta, \omega_0 + 4\Delta, \omega_0 + 3\Delta)$ with $\omega_0/2\pi \in [6, 10]$ GHz and $\Delta/2\pi \in [0.5, 1]$ GHz. With current level of technology, such configuration can be realized with very high precision through the design and fabrication of the circuit (e.g. length selection or impedance engineering) [45, 50].

The second function of the grounding SQUIDs is to implement the effective Hamiltonian

$$\mathcal{H}_T = \sum_{\langle (\mathbf{r}, \alpha), (\mathbf{r}', \beta) \rangle} \mathcal{T}_{\mathbf{r}, \alpha}^{\mathbf{r}', \beta} \beta_{\mathbf{r}'}^\dagger \alpha_{\mathbf{r}} e^{i\theta_{\mathbf{r}, \alpha}^{\mathbf{r}', \beta}} + \text{H.C.}, \quad (2)$$

in the rotating frame of \mathcal{H}_S through the PFC method. Here $\mathcal{T}_{\mathbf{r}, \alpha}^{\mathbf{r}', \beta}$ labels the real $(\mathbf{r}, \alpha) \Leftrightarrow (\mathbf{r}', \beta)$ hopping strength sketched in Fig. 1a, and $\theta_{\mathbf{r}, \alpha}^{\mathbf{r}', \beta} = \int_{\mathbf{r}, \alpha}^{\mathbf{r}', \beta} d\mathbf{x} \cdot \mathbf{A}(\mathbf{x})$ is the corresponding hopping phase manifesting the existence of the vector potential $\mathbf{A}(\mathbf{x})$ [51]. We establish Eq. (2) through the dynamic modulation of the grounding SQUIDs [32, 42, 45]. The physics can be briefly illustrated in the following two steps:

1. Let us consider a particular neighboring TLR pair $\langle (\mathbf{r}, \alpha), (\mathbf{r}', \beta) \rangle$. Due to the very small inductances of their common grounding SQUID, the voltage across the SQUID is very small, and the grounding SQUID works effectively as a linear inductance which can be tuned by its penetrated flux. As the currents of the two TLRs flow through the same grounding SQUID, an inductive current-current coupling

$$\mathcal{H}_S^{\mathbf{r}\alpha, \mathbf{r}'\beta} = \mathcal{T}_{\mathbf{r}\alpha, \mathbf{r}'\beta}^{\text{ac}}(t)(\alpha_{\mathbf{r}} + \alpha_{\mathbf{r}}^\dagger)(\beta_{\mathbf{r}'} + \beta_{\mathbf{r}'}^\dagger), \quad (3)$$

can be induced, with the time-dependent coupling constant $\mathcal{T}_{\mathbf{r}\alpha, \mathbf{r}'\beta}^{\text{ac}}(t)$ proportional to the Josephson coupling energy (and consequently controlled by the penetrated flux) of the grounding SQUID. We

then a.c. modulate the grounding SQUID with frequency bridging the frequency gap between the two TLRs. With this modulation, a PFC process between the TLRs can be induced, described in the rotating frame of \mathcal{H}_S by

$$\mathcal{H}_T^{\mathbf{r}\alpha, \mathbf{r}'\beta} = \mathcal{T}_{\mathbf{r}, \alpha}^{\mathbf{r}', \beta} \beta_{\mathbf{r}'}^\dagger \alpha_{\mathbf{r}} e^{i\theta_{\mathbf{r}, \alpha}^{\mathbf{r}', \beta}} + \text{H.C.}, \quad (4)$$

where the hopping amplitude $\mathcal{T}_{\mathbf{r}, \alpha}^{\mathbf{r}', \beta}$ is proportional to the amplitude of the modulating tone, and the hopping phase $\theta_{\mathbf{r}, \alpha}^{\mathbf{r}', \beta}$ is exactly the initial phase of the modulating tone. If we want to induce the on-site term, we merely need to adjust the modulating frequency and choose a corresponding different rotating frame. With reported experimental data [32, 41, 44–46], the hopping strength $\mathcal{T}_{\mathbf{r}, \alpha}^{\mathbf{r}', \beta}$ can further be estimated as $\mathcal{T}_{\mathbf{r}, \alpha}^{\mathbf{r}', \beta} \in [5, 15]$ MHz. Moreover, previous discussions [42, 43] have suggested that such PFC formalism is robust against the fabrication error and the $1/f$ noise in SQC [52], implying that the $\mathcal{H}_T^{\mathbf{r}\alpha, \mathbf{r}'\beta}$ term can be stably and precisely synthesized.

2. We then generalize the described PFC method to each of the hopping link on the lattice: We modulate each of the grounding SQUIDs on the lattice with pulses containing three tones Δ , 2Δ , and 4Δ . A close inspection indicates that we can independently control every vertical hopping branch and every pair of horizontal hopping branches by a modulating tone threaded in one of the grounding SQUIDs [42]. The summation of all these hopping terms thus leads to the establishment of the effective Hamiltonian in Eq. (2) with time- and site-resolved tunability. In particular, the site-dependent hopping strength meets the requirement of inhomogeneous hopping amplitudes, which is important for the 2D SSH lattice to enter the topological non-trivial region [3, 53], while the controllable hopping phases pinpoint the creation of arbitrary synthetic magnetic field with Landau gauge for microwave photons.

III. HIGH ORDER TOPOLOGICAL PHASES VERSUS VARYING MAGNETIC FIELD IN 2D SSH LATTICE

Currently the detailed-and-ultimate characterization of high order band topology in the presence of magnetic field is still under debate [1, 6, 11–13, 47]. Motivated by the principle of bulk-edge correspondence [7], we follow an alternative route of investigation in this manuscript, that is, to study the boundary behavior of the lattice. In the rest of this manuscript, we consider the corner excitation physics on a cQED lattice consisting of 8×8 unit-cells (i.e. 16×16 sites). In the first situation, we consider the uniform inter-cell hopping and set λ_i as unity, i. e.

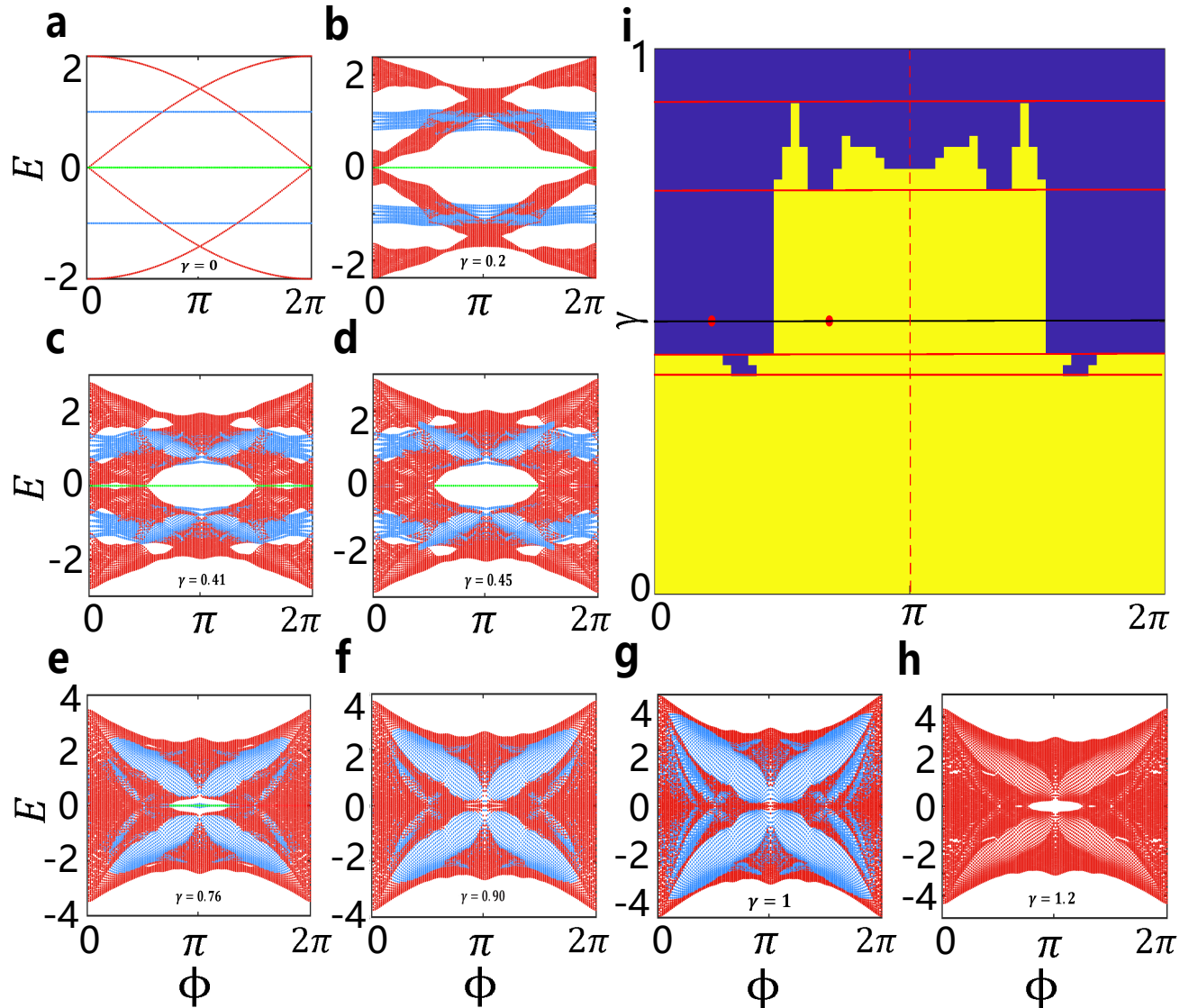


FIG. 2. **a - h** Numerically simulated HBS under OBC for varying γ . The bulk, edge, and corner modes are labelled by the red, blue, and green lines, respectively. **i** HOTI phase diagram of the lattice. Here we characterize the topological trivial/non-trivial region simply by the absence/existence of the ZECMs, and label them by the blue/yellow colors, respectively. The phase diagram is mirror-symmetric with respect to $\phi = \pi$ (the red dashed line). The red solid lines denote the gap closing points $\gamma_{c1} = 0.41$, $\gamma_{c2} = 0.45$, $\gamma_{c3} = 0.76$, and $\gamma_{c4} = 0.90$ from bottom to top (see main text for details). The black line with red dots at $\phi = 2\pi/3$ and $\phi = 2\pi/10$ is $\gamma = 0.5$ which is used for the numerical simulation in Sec. IV.

$\lambda_i = 1$ for $i = 1, 2, 3, 4$. The intra-cell hopping strength γ and the magnetic flux ϕ is set in the range $\gamma \in [0, 1.2]$ and $\phi \in [0, 2\pi]$, respectively. The Hofstadter butterfly energy spectrum (HBS) under open boundary condition (OBC) is calculated and shown in Fig. 2 (the truncation is placed between the unit-cells). Compared with that under periodic boundary condition, the HBS under OBC has edge modes (blue lines) and ZECMs (green lines) emerged from the bulk modes (red lines). In what follows, we characterize the topology of the considered lattice by the behavior of the ZECMs. As shown in Fig. 2,

the HBS and the topological phase of the lattice versus γ and ϕ can be generally divided into five situations (here we only describe the range $\phi \in [0, \pi]$ because the HBS exhibits mirror symmetry with respect to $\phi = \pi$):

1. As shown in Fig. 2a, The HBS at $\gamma = 0$ can be classified into bulk, edge, and corner state. The eigenvalues of the edge states are 28-fold degenerate in our 8×8 unit-cells, with the degeneracy depending on the lattice size, while the zero eigenvalue of the corner states are four-fold degenerate, with the degeneracy irrelevant of the lattice size. The ex-

istence of the ZECMs pinpoints that the 2D SSH model now is a non-trivial HOTI. As γ increases in the range $\gamma \in (0, 0.41)$ (Fig. 2b), the degeneracy of the edge states is destroyed and the energy band of the edge states becomes broad. Meanwhile, the corner states still remain zero-energy and four-fold degenerate. The band gap at $E = 0$ between the bulk modes and the ZECMs exists in all range of ϕ and decreases with increasing γ , implying that the HOTI phase now is robust against the imposed magnetic fields. Here the upper bound $\gamma_{c1} = 0.41$ (and the lower and upper bounds in the other situations) is not an analytic result but obtained numerically.

2. As γ passes the point $\gamma_{c1} = 0.41$ and varies in the range $\gamma \in [0.41, 0.45]$, the band gap and consequently the ZECMs always exist for $\phi \in [\pi/2, \pi]$. However, the band gap is closed at points located in $\phi \in [0, \pi/2]$ (Fig. 2c). Here the gap-closing is not complete in the sense that the gap is not closed for all $\phi \in [0, \pi/2]$. The ZECMs in this range behaves much more complicated: the ZECMs still exist for those ϕ where the band gap is still open. Meanwhile, for those ϕ where the band gap is closed, the ZECMs may either disappear or even co-exist with the bulk modes.
3. After γ goes across the point $\gamma_{c2} = 0.45$ and moves into the range $\gamma \in [0.45, 0.76]$, the band gap closes completely in the range $\phi \in [0, \pi/2]$ but still exist in the whole range of $\phi \in [\pi/2, \pi]$, as shown in Fig. 2d. The band width of the edge state now becomes larger, and approaches the zero-energy value in the range $\phi \in [0, \pi/2]$. Meanwhile, the ZECMs exist in the whole range of $\phi \in [\pi/2, \pi]$ and disappear completely in the whole range of $\phi \in [0, \pi/2]$. It implies that the system with $0 < \phi < \pi/2$ can not be continuously deformed into that with $\pi/2 < \phi < \pi$ due to the gap-closing at the $\phi = \pi/2$ [11, 12], and pinpoint a HOTI phase transition occurring at $\phi = \pi/2$.
4. For γ in the range $\gamma \in [0.76, 0.90]$, the band gap closes completely in the range $\phi \in [0, \pi/2]$ and incompletely in $\phi \in [\pi/2, \pi]$. With increasing γ , the band gap shrinks continuously and eventually vanishes at $\gamma_{c4} = 0.90$ (Figs. 2e and 2f).
5. Finally, in the range $\gamma > 0.90$, the band gap near $E = 0$ is reopened in the range $\phi \in [\pi/2, \pi]$. The ZECMs, however, disappear. The absence of the ZECMs imply that now the lattice is in the topological trivial phase (Figs. 2g and 2h).

As a summary of the above results, we further plot in Fig. 2i the HOTI phase diagram of the lattice. Notice that our result is consistent with previous work which considered only several discrete values of ϕ [11]. Here we label the trivial/non-trivial HOTI phases simply by the existence of the ZECMs.

IV. MEASUREMENT SCHEME OF THE PROPOSED HOTI PHASE

In the next step, we consider the measurement scheme of the proposed topological phases. With current level of technology, the measurement of HBS of small-size lattice has been reported [33]. However, this method can hardly be generalized to large-scale lattice, because the energy spacing becomes much more dense with increasing lattice size. Therefore, we consider the observation scheme based on the corner site excitation of the proposed lattice. The motivate is that the proposed high order topology is characterized by the behavior of the ZECMs and the ZECMs are spatially localized near the corners and spectrally located at $E = 0$. We can capacitively couple external pump coil to the corner sites (Fig. 1b) and inject pulses matching the zero frequency in the rotating frame of \mathcal{H}_S . If the ZECMs exist, the response of the lattice will accordingly exhibit spatially localized patterns, otherwise the response will extend over a wide range on the lattice. In this sense, we can determine the existence of the ZECMs and consequently the topology of the lattice by measuring merely few sites near the corners. Two candidate physical observables can be considered. The first one is the SSPN: We pump the corner sites for sufficiently long time and let the lattice approach its steady state. Then the SSPN of the corner sites and its few neighbors can be determined by measuring the energy leaking out (Fig. 1b). The second one is the reflection coefficient: We input a pulse into the corner site and measure the output photon currents from the corner sites and their neighbors. Based on the input-output formalism [54], the spatial and spectral distribution of the ZECMs can be determined from the reflected signals. Both these two schemes have been reported in recent experiments [55, 56]. In the following, we perform numerical simulations following the SSPN scheme: The coherent monochromatic pumping of a particular single-site (\mathbf{r}_p, α) can be described by

$$\mathcal{H}_{\text{pump}} = \mathcal{P}^\dagger \mathbf{a} e^{-i\Omega_P t} + \text{h.c.}, \quad (5)$$

where \mathcal{P} is the pumping strength vector with only one non-zero element at (\mathbf{r}_p, α) , \mathbf{a} is the vector of annihilation operators of the lattice sites, and Ω_P is the detuning of the pumping frequency in the rotating frame of \mathcal{H}_S . The SSPN of the lattice can be obtained through the equation [43]

$$i \frac{d\langle \mathbf{a} \rangle}{dt} = \left[\mathcal{B} - \left(\Omega_P + \frac{1}{2} i\kappa \right) \mathcal{I} \right] \langle \mathbf{a} \rangle + \mathcal{P} = 0, \quad (6)$$

where the matrix \mathcal{B} is defined by $\mathbf{a}^\dagger \mathcal{B} \mathbf{a} = \mathcal{H}_T$. Without loss of generality here we assume that the TLRs have uniform decay rate κ .

Suppose (\mathbf{r}_c, β) is a corner site, we can measure the SSPN $n_{\mathbf{r}_c, \beta} = \langle \beta_{\mathbf{r}_c}^\dagger \beta_{\mathbf{r}_c} \rangle$ at exactly this site, and the summation of SSPN at (\mathbf{r}_c, β) and its few neighbors, which we denote as $N_{\mathbf{r}_c, \beta}$. Then the concentration factor $R_{\mathbf{r}_c, \beta} = n_{\mathbf{r}_c, \beta} / N_{\mathbf{r}_c, \beta}$ serves as a good index of the

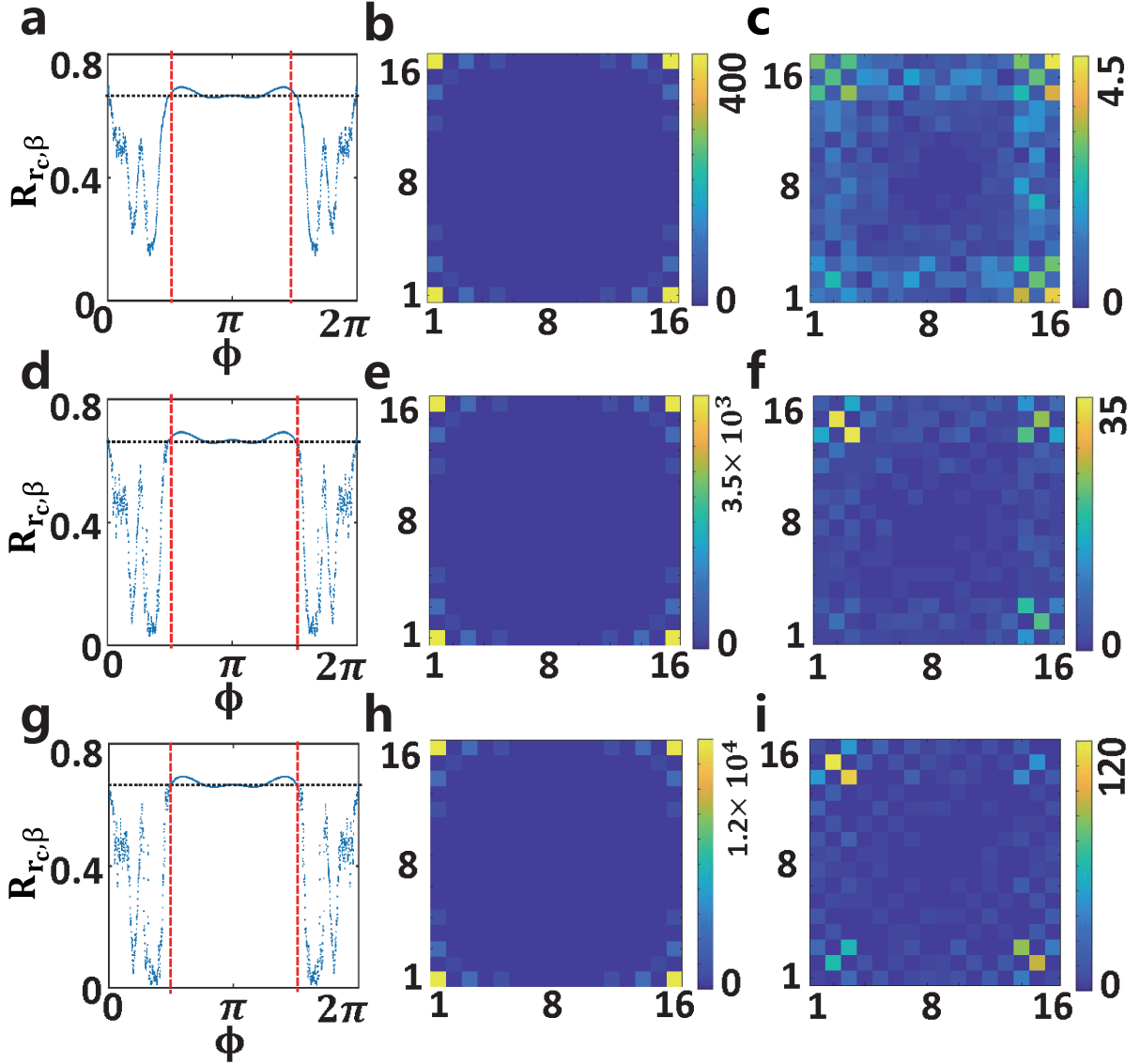


FIG. 3. Numerically simulated SSPN distributions versus magnetic field ϕ and dissipation factor κ . **a** depicts the concentration factor $R_{\mathbf{r}_c, \beta}$ at $\kappa = 0.03$. Here the summation $N_{\mathbf{r}_c, \beta}$ is performed at the corner sites and their nearest six neighbors indicated by the dashed triangle in Fig. 1a. The red vertical dashed lines denote the topological phase transition points $\phi = \pi/2$ and $\phi = 3\pi/2$, and the black horizontal dotted line labels the empirical critical value $R_{\mathbf{r}_c, \beta} = 0.7$. The SSPNs distribution of the whole lattice at $\phi = 2\pi/3$ and $\phi = 2\pi/10$ are sketched in **b** and **c**, respectively. **d-f** and **g-i** show the same calculations at $\kappa = 0.01$ and $\kappa = 0.005$, respectively.

existence of the ZECMs. A significant high $R_{\mathbf{r}_c, \beta}$ can be obtained only if the following three requirements are met simultaneously: 1. the ZECMs do exist, i.e. the lattice is in its topological non-trivial phase. 2. $(\mathbf{r}_c, \beta) = (\mathbf{r}_p, \alpha)$, i.e. what we pump is a corner site. 3. $\Omega_P \approx 0$. Only in this situation can the ZECMs be effectively excited, and the injected photons will prefer locating on the corner site (\mathbf{r}_c, β) . Otherwise, we will have very low $R_{\mathbf{r}_c, \beta}$: If the ZECMs do not exist, we can only excite the spatially extended bulk or edge modes if Ω_P is in the bulk or edge bands, leading to the dilution of the weight of SSPN on

(\mathbf{r}_c, β) , or even can not effectively excite the lattice if Ω_P is in the gap; if the ZECMs exist but we either do not pump the corner sites or pump the corner sites with $\Omega_P \neq 0$, our pumping is not compatible with the ZECMs and thus can not effectively excite the ZECMs.

We perform our numerical simulation based on several recently reported experiments [57–59] and show our results in Fig. 3a-c. Here we choose $\kappa = 0.03$ and set $\gamma = 0.5$, $\lambda_i = 1$ following our previous analysis in Sec. III (see also Fig. 2i). To detect the ZECMs, we set $\Omega_P = 0$ and choose $\mathcal{P}^\dagger \mathbf{a} = A_{1,1} + B_{1,8} + C_{8,1} + D_{8,8}$ (here we

simulate the four-site pumping for better visualization. This choice does not affect our discussion and conclusion because the four single-site pumpings can be regarded as independent due to their distant spacing). We observe that $R_{\mathbf{r}_c, \beta}$ jumps dramatically at $\pi/2$ as shown in Fig. 3a. This jump is a clear evidence of the predicted topological phase transition induced by varying ϕ at $\phi = \pi/2$. In addition, our numerical calculation implies that $R_{\mathbf{r}_c, \beta} > 0.7$ can serve as for the existence of the ZECMs. To better visualize the influence of the magnetic field ϕ , we plot the SSPN of the whole lattice with topological non-trivial $\phi = 2\pi/3$ and topological trivial $\phi = 2\pi/10$ in Fig. 3b and c, respectively. The localization of the SSPN at $\phi = 2\pi/3$ and its diffusion at $\phi = 2\pi/10$ can be clearly identified.

Here we offer a brief remark on the influence of the dissipation factor κ on the localization of the photons. As the dissipation can also hinder the diffusion of the photons, we should discriminate whether the observed localization is caused by the appearance of ZECMs or by the dissipation of the lattice. Therefore, we consider the behavior of $R_{\mathbf{r}_c, \beta}$ and the SSPN under different κ . If their behavior is basically unchanged, we can conclude that the localization of the SSPNs is indeed caused by the appearance of ZECMs. We then perform the same numerical simulation with $\kappa = 0.01$ and $\kappa = 0.005$, and show the corresponding results in Figs. 3d-f and 3g-i, respectively. With decreasing κ , the obtained results are largely unchanged, indicating that the observed localization is indeed caused by the appearance of ZECMs. Moreover, the jump of $R_{\mathbf{r}_c, \beta}$ at $\phi = \pi/2$ becomes increasingly sharp, and the SSPN at the topological trivial becomes more diffused. Therefore, smaller dissipation can help us to better identify the topological trivial/non-trivial regions. Meanwhile, as indicated in Fig. 3a, a moderate, currently achievable $\kappa = 0.03$ is already sufficient for the discrimination the phase boundary.

Our proposed architecture can also be used to verify the anisotropy-induced HOTI predicted in Ref. [53]. Here we set $\phi = \pi, \gamma = 1$, and $\lambda_2 = \lambda_3 = 3$. The HOTI phase diagram of the lattice versus λ_1 and λ_4 is shown in Fig. 4a. In particular, the yellow, green and blue regions label different polarization vectors [1] $\mathbf{P} = (0, 0)$, $\mathbf{P} = (0, 1/2)$ (upper left) or $\mathbf{P} = (1/2, 0)$ (lower right), and $\mathbf{P} = (1/2, 1/2)$, respectively. These different polarization vectors in turn correspond to different numbers and locations of the ZECMs. The energy spectrum of the lattice at several representative points are calculated and shown in Fig. 4b-d: In the yellow region the lattice has four ZECMs locating at the four corners, while in the green region the lattice has two ZECMs, the location of which depending on λ_1/λ_4 ; However, the lattice has only extended bulk and edge modes but no isolated ZECMs in the blue region.

We further numerically calculate the SSPN distribution of the lattice at these four representative points with $\kappa = 0.03$, $\Omega_P = 0$, and $\mathcal{P}^\dagger \mathbf{a} = A_{1,1} + B_{1,8} + C_{8,1} + D_{8,8}$. In Fig. 4e, we choose $\lambda_1 = \lambda_4 = 3$. We find that the SSPN

is localized at four corners, indicating that there exist four ZECMs locating at the four corners. This is consistent with the spectrum shown in Fig. 4b. Meanwhile, in Fig. 4f with $\lambda_1 = 3$ and $\lambda_4 = 0.5$, the resulting SSPN is localized only at two adjacent corner sites along the horizontal direction at the bottom. The SSPN distribution implies there exists only two ZECMs, which is consistent with Fig. 4f. In Fig. 4g, with inversely chosen $\lambda_1 = 0.5$ and $\lambda_4 = 3$, the SSPN is localized at two adjacent corner sites along vertical direction. The comparison between Fig. 4f and 4g manifests their different polarization vectors. Finally, in Fig. 4h we choose $\lambda_1 = \lambda_4 = 0.5$. Now the SSPN is no longer localized at the corner sites, implying that there is no ZECMs. These calculated SSPN distributions thus confirm the validity of our method, that is, we can extract the spatial and spectral information of the ZECMs by pumping the corner sites and detecting the corner sites and their few neighbors. Here we notice that our result is consistent with the previous theoretical work which states that the high order topological property is protected by the chiral symmetry and is not dependent on any spatial symmetry. [53].

V. CONCLUSION AND OUTLOOK

In conclusion, we have shown that it is not only possible, but also advantageous to implement and detect the HOTI phase transition of 2D SSH lattice induced by continuous magnetic field in SQC system. Meanwhile, it is our feeling that we are still in the beginning of this research direction. Due to the flexibility of the cQED architecture, we can expect that other HOTI lattice configuration (e.g. kagome and honeycomb [6, 47]) can also be established by using our method. Moreover, the PFC method allows the further combination with many other mechanisms, including on-site Hubbard interaction [27, 39], disorder, and non-Hermiticity [48, 49]. In particular, the reduction of the fabrication error of cQED elements can be exploited to suppress and controllably introduce the mechanism of disorder [50]. Another expectation comes from the fact that the effective photon-photon interaction, i.e. the nonlinearity of microwave photons can be incorporated into cQED system in a variety of manners, including the electromagnetically induced transparency [35], Jaynes-Cummings-Hubbard nonlinearity [36], and nonlinear Josephson coupling [60, 61]. Our third perspective comes from the fact that the decoherence in superconducting quantum circuit can now be suppressed and efficiently controlled [62]. This technique can be used to manipulate the gain and loss of the system, leading to the quantum simulation of non-Hermitian HOTI [63, 64]. Therefore, our further direction should be the interplay of the above mentioned mechanism in our proposed architecture, which will bring us into the realm of rich but less-explored physics.

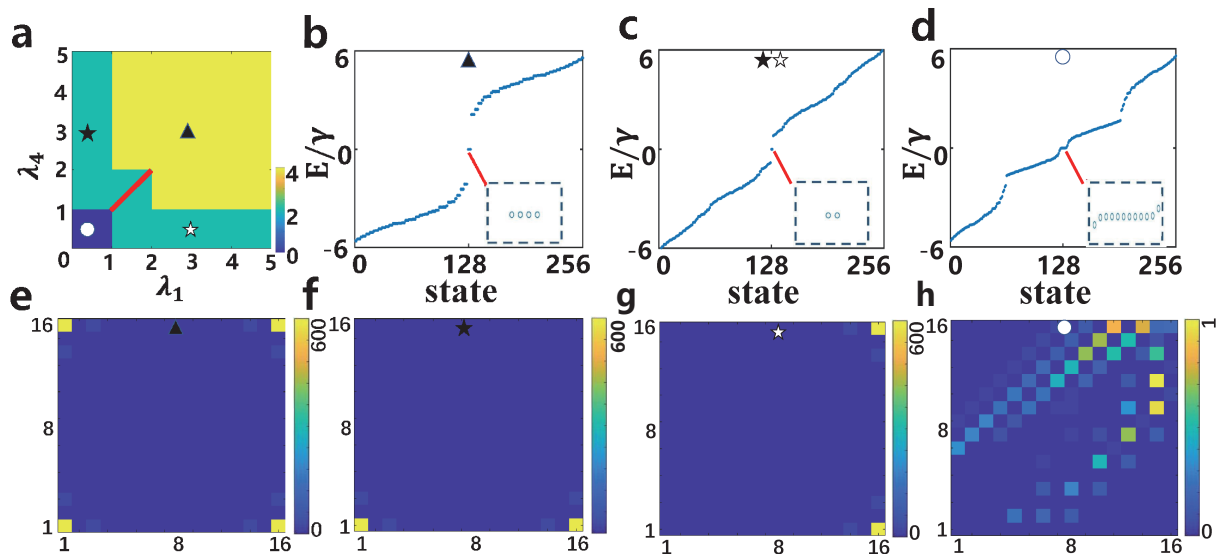


FIG. 4. **a** HOTI phase diagram of the 2D SSH lattice with $\phi = \pi$, $\gamma = 1$ and $\lambda_2 = \lambda_3 = 3$. The phases are labelled by different colors indicating the number of the corner modes. In the blue, green, and yellow regions, the lattice have polarization vectors $\mathbf{P} = (0, 0)$, $\mathbf{P} = (0, 1/2)$ (upper left) or $\mathbf{P} = (1/2, 0)$ (lower right), and $\mathbf{P} = (1/2, 1/2)$ and consequently zero, two, and four ZECMs, respectively. The spectra of the lattice at several representative points, labelled by triangle: $\lambda_1 = \lambda_4 = 3$, star: $\lambda_1 = 3$, $\lambda_4 = 0.5$, hollowed star: $\lambda_1 = 0.5$, $\lambda_4 = 3$ and round: $\lambda_1 = \lambda_4 = 0.5$, are shown in **b - d**, respectively. The spectrum behavior around the zero energy are detailed in the insets. The corresponding SSPN distributions under $\kappa = 0.03$, $\Omega_P = 0$, and $\mathcal{P}^\dagger \mathbf{a} = A_{1,1} + B_{1,8} + C_{8,1} + D_{8,8}$ are shown in **e - h**, respectively.

ACKNOWLEDGMENTS

We thank Y. H. Wu for helpful discussion. This work was supported in part by the National Science Founda-

tion of China (Grants No. 11774114, No. 11874156, and No. 11874160).

-
- [1] W. A. Benalcazar, B. A. Bernevig, and T. L. Hughes, *Science* **357**, 61 (2017).
 - [2] F. Schindler, A. M. Cook, M. G. Vergniory, Z. Wang, S. S. P. Parkin, B. A. Bernevig, and T. Neupert, *Sci. Adv.* **4** (2018).
 - [3] Z. Song, Z. Fang, and C. Fang, *Phys. Rev. Lett.* **119**, 246402 (2017).
 - [4] W. A. Benalcazar, B. A. Bernevig, and T. L. Hughes, *Phys. Rev. B* **96**, 245115 (2017).
 - [5] J. Langbehn, Y. Peng, L. Trifunovic, F. von Oppen, and P. W. Brouwer, *Phys. Rev. Lett.* **119**, 246401 (2017).
 - [6] M. Ezawa, *Phys. Rev. Lett.* **120**, 026801 (2018).
 - [7] A. B. Bernevig and T. L. Hughes, *Topological Insulators and Topological Superconductor* (Princeton University Press, Princeton and Oxford, 2013).
 - [8] S. Franca, J. van den Brink, and I. C. Fulga, *Phys. Rev. B* **98**, 201114 (2018).
 - [9] F. Liu and K. Wakabayashi, *Phys. Rev. Lett.* **118**, 076803 (2017).
 - [10] M. Kim and J. Rho, *Topological edge and corner states in a two-dimensional photonic SSH lattice* (2019), arXiv:1909.01037.
 - [11] Y. Otaki and T. Fukui, *Phys. Rev. B* **100**, 245108 (2019).
 - [12] J. Herzog-Arbeitman, Z.-D. Song, N. Regnault, and B. A. Bernevig, *Phys. Rev. Lett.* **125**, 236804 (2020).
 - [13] M. Rodriguez-Vega, A. Kumar, and B. Seradjeh, *Phys. Rev. B* **100**, 085138 (2019).
 - [14] E. Khalaf, W. A. Benalcazar, T. L. Hughes, and R. Queiroz, *Phys. Research* **3**, 013239 (2021).
 - [15] I. M. Georgescu, S. Ashhab, and F. Nori, *Rev. Mod. Phys.* **86**, 153 (2014).
 - [16] T. Ozawa, H. M. Price, A. Amo, N. Goldman, M. Hafezi, L. Lu, M. C. Rechtsman, D. Schuster, J. Simon, O. Zeitlinger, and I. Carusotto, *Rev. Mod. Phys.* **91**, 015006 (2019).
 - [17] L. Lu, J. D. Joannopoulos, and M. Soljacic, *Nat. Photon.* **8**, 821 (2014).
 - [18] M. Ezawa, *Phys. Rev. B* **99**, 201411 (2019).
 - [19] B.-Y. Xie, G.-X. Su, H.-F. Wang, H. Su, X.-P. Shen, P. Zhan, M.-H. Lu, Z.-L. Wang, and Y.-F. Chen, *Phys. Rev. Lett.* **122**, 233903 (2019).
 - [20] X.-D. Chen, W.-M. Deng, F.-L. Shi, F.-L. Zhao, M. Chen, and J.-W. Dong, *Phys. Rev. Lett.* **122**, 233902 (2019).
 - [21] B.-Y. Xie, H.-F. Wang, H.-X. Wang, X.-Y. Zhu, J.-H. Jiang, M.-H. Lu, and Y.-F. Chen, *Phys. Rev. B* **98**, 205147 (2018).

- [22] M. Serra-Garcia, V. Peri, R. Susstrunk, O. R. Bilal, T. Larsen, L. G. Villanueva, and S. D. Huber, *Nature* **555**, 342 (2018).
- [23] C. W. Peterson, W. A. Benalcazar, T. L. Hughes, and G. Bahl, *Nature* **555**, 346 (2018).
- [24] S. Imhof, C. Berger, F. Bayer, J. Brehm, L. W. Molenkamp, T. Kiessling, F. Schindler, C. H. Lee, M. Greiter, T. Neupert, and R. Thomale, *Nat. Phys.* **14**, 925 (2018).
- [25] M. Serra-Garcia, R. Süssstrunk, and S. D. Huber, *Phys. Rev. B* **99**, 020304 (2019).
- [26] I. Carusotto, A. A. Houck, A. J. Kollár, P. Roushan, D. I. Schuster, and J. Simon, *Nature Physics* **16**, 268 (2020).
- [27] S. Schmidt and J. Koch, *Ann. Phys.* **525**, 395 (2013).
- [28] A. Blais, A. L. Grimsmo, S. M. Girvin, and A. Wallraff, *Rev. Mod. Phys.* **93**, 025005 (2021).
- [29] J. M. Martinis, M. H. Devoret, and J. Clarke, *Nat. Phys.* **16**, 234 (2020).
- [30] J. M. Martinis and M. R. Geller, *Phys. Rev. A* **90**, 022307 (2014).
- [31] J. Stehlik, D. M. Zajac, D. L. Underwood, T. Phung, J. Blair, S. Carnevale, D. Klaus, G. A. Keefe, A. Carniol, M. Kumph, M. Steffen, and O. E. Dial, *Phys. Rev. Lett.* **127**, 080505 (2021).
- [32] P. Roushan, C. Neill, A. Megrant, Y. Chen, R. Babbush, R. Barends, B. Campbell, Z. Chen, B. Chiaro, A. Dunsworth, A. Fowler, E. Jeffrey, J. Kelly, E. Lucero, J. Mutus, P. J. J. O'Malley, M. Neeley, C. Quintana, D. Sank, A. Vainsencher, J. Wenner, T. White, E. Kapit, H. Neven, and J. Martinis, *Nat. Phys.* **13**, 146 (2017).
- [33] P. Roushan, C. Neill, J. Tangpanitanon, V. M. Bastidas, A. Megrant, R. Barends, Y. Chen, Z. Chen, B. Chiaro, A. Dunsworth, A. Fowler, B. Foxen, M. Giustina, E. Jeffrey, J. Kelly, E. Lucero, J. Mutus, M. Neeley, C. Quintana, D. Sank, A. Vainsencher, J. Wenner, T. White, H. Neven, D. G. Angelakis, and J. Martinis, *Science* **358**, 1175 (2017).
- [34] X. Gu, A. F. Kockum, A. Miranowicz, Y.-X. Liu, and F. Nori, *Phys. Rep.* **718-719**, 1 (2017).
- [35] M. J. Hartmann, F. G. S. L. Brandão, and M. B. Plenio, *Nat. Phys.* **2**, 849 (2006).
- [36] A. D. Greentree, C. Tahan, J. H. Cole, and L. C. L. Hollenberg, *Nat. Phys.* **2**, 856 (2006).
- [37] I. Carusotto, D. Gerace, H. E. Tureci, S. De Liberato, C. Ciuti, and A. Imamoglu, *Phys. Rev. Lett.* **103**, 033601 (2009).
- [38] A. L. C. Hayward, A. M. Martin, and A. D. Greentree, *Phys. Rev. Lett.* **108**, 223602 (2012).
- [39] I. Carusotto and C. Ciuti, *Rev. Mod. Phys.* **85**, 299 (2013).
- [40] R. Ma, B. Saxberg, C. Owens, N. Leung, Y. Lu, J. Simon, and D. I. Schuster, *Nature* **566**, 51 (2019).
- [41] E. Zakka-Bajjani, F. Nguyen, M. Lee, L. R. Vale, R. W. Simmonds, and J. Aumentado, *Nat. Phys.* **7**, 599 (2011).
- [42] Y.-P. Wang, W.-L. Yang, Y. Hu, Z.-Y. Xue, and Y. Wu, *NPJ Quantum Inf.* **2**, 16015 (2016).
- [43] Z.-H. Yang, Y.-P. Wang, Z.-Y. Xue, W.-L. Yang, Y. Hu, J.-H. Gao, and Y. Wu, *Phys. Rev. A* **93**, 062319 (2016).
- [44] F. Nguyen, E. Zakka-Bajjani, R. W. Simmonds, and J. Aumentado, *Phys. Rev. Lett.* **108**, 163602 (2012).
- [45] J. S. C. Hung, J. H. Busnaina, C. W. S. Chang, A. M. Vadiraj, I. Nsanzineza, E. Solano, H. Alaeian, E. Rico, and C. M. Wilson, *Phys. Rev. Lett.* **127**, 100503 (2021).
- [46] C. M. Wilson, G. Johansson, A. Pourkabirian, M. Simoen, J. R. Johansson, T. Duty, F. Nori, and P. Delsing, *Nature* **479**, 376 (2011).
- [47] F. Liu, H.-Y. Deng, and K. Wakabayashi, *Phys. Rev. Lett.* **122**, 086804 (2019).
- [48] E. J. Bergholtz, J. C. Budich, and F. K. Kunst, *Rev. Mod. Phys.* **93**, 015005 (2021).
- [49] Y. Ashida, Z. Gong, and M. Ueda, *Advances in Physics* **69**, 249 (2020), <https://doi.org/10.1080/00018732.2021.1876991>.
- [50] D. L. Underwood, W. E. Shanks, J. Koch, and A. A. Houck, *Phys. Rev. A* **86**, 023837 (2012).
- [51] N. Goldman, G. Juzeliūnas, Pohberg, and I. B. Spielman, *Rep. Prog. Phys.* **77**, 126401 (2014).
- [52] E. Paladino, Y. M. Galperin, G. Falci, and B. L. Altshuler, *Rev. Mod. Phys.* **86**, 361 (2014).
- [53] L. Li, M. Umer, and J. Gong, *Phys. Rev. B* **98**, 205422 (2018).
- [54] A. A. Clerk, M. H. Devoret, S. M. Girvin, F. Marquardt, and R. J. Schoelkopf, *Rev. Mod. Phys.* **82**, 1155 (2010).
- [55] A. J. Sirois, M. A. Castellanos-Beltran, M. P. DeFeo, L. Ranzani, F. Lecocq, R. W. Simmonds, J. D. Teufel, and J. Aumentado, *Appl. Phys. Lett.* **106**, 172603 (2015).
- [56] B. J. Chapman, E. I. Rosenthal, J. Kerckhoff, B. A. Moores, L. R. Vale, J. A. B. Mates, G. C. Hilton, K. Lalumière, A. Blais, and K. W. Lehnert, *Phys. Rev. X* **7**, 041043 (2017).
- [57] Z. Wang, Y. Wu, Z. Bao, Y. Li, C. Ma, H. Wang, Y. Song, H. Zhang, and L. Duan, *Phys. Rev. Applied* **15**, 014049 (2021).
- [58] M. Mergenthaler, A. Nersisyan, A. Patterson, M. Esposito, A. Baumgartner, C. Schönenberger, G. A. D. Briggs, E. A. Laird, and P. J. Leek, *Phys. Rev. Applied* **15**, 064050 (2021).
- [59] X. Tan, Y. X. Zhao, Q. Liu, G. Xue, H.-F. Yu, Z. D. Wang, and Y. Yu, *Phys. Rev. Lett.* **122**, 010501 (2019).
- [60] J. Bourassa, F. Beaudoin, J. M. Gambetta, and A. Blais, *Phys. Rev. A* **86**, 013814 (2012).
- [61] M. Leib, F. Deppe, A. Marx, R. Gross, and M. Hartmann, *New J. Phys.* **14**, 075024 (2012).
- [62] M. Naghiloo, M. Abbasi, Y. N. Joglekar, and K. W. Murch, *Nature Physics* **15**, 1232 (2019).
- [63] T. Liu, Y.-R. Zhang, Q. Ai, Z. Gong, K. Kawabata, M. Ueda, and F. Nori, *Phys. Rev. Lett.* **122**, 076801 (2019).
- [64] X.-W. Luo and C. Zhang, *Phys. Rev. Lett.* **123**, 073601 (2019).